Philosophical Magazine
Publication details, including instructions for authors and subscription information:
http://www.tandfonline.com/loi/tphm20

A study on the formation of crystalline phases during solidification and crystallisation in the bulk metallic glass of $Zr_{53}Cu_{21}Al_{10}Ni_8Ti_8$ composition

S. Neogy [a], R. Tewari [a], G.K. Dey [a], S. Banerjee [a] & S. Ranganathan [b]

[a] Materials Science Division, Bhabha Atomic Research Centre, Mumbai 400 085, India

[b] Department of Metallurgy, Indian Institute of Science, Bangalore 560 012, India

Published online: 02 Apr 2012.

To cite this article: S. Neogy, R. Tewari, G.K. Dey, S. Banerjee & S. Ranganathan (2012) A study on the formation of crystalline phases during solidification and crystallisation in the bulk metallic glass of $Zr_{53}Cu_{21}Al_{10}Ni_8Ti_8$ composition, Philosophical Magazine, 92:17, 2136-2149, DOI: 10.1080/14786435.2012.669061

To link to this article: http://dx.doi.org/10.1080/14786435.2012.669061

Philosophical Magazine
Vol. 92, No. 17, 11 June 2012, 2136–2149

Taylor & Francis
Taylor & Francis Group

A study on the formation of crystalline phases during solidification and crystallisation in the bulk metallic glass of $Zr_{53}Cu_{21}Al_{10}Ni_8Ti_8$ composition

S. Neogy[a], R. Tewari[a]*, G.K. Dey[a], S. Banerjee[a] and S. Ranganathan[b]

[a]*Materials Science Division, Bhabha Atomic Research Centre, Mumbai 400 085, India;* [b]*Department of Metallurgy, Indian Institute of Science, Bangalore 560 012, India*

(*Received 31 May 2011; final version received 18 February 2012*)

The present paper considers the formation of crystalline phases during solidification and crystallisation of the $Zr_{53}Cu_{21}Al_{10}Ni_8Ti_8$ alloy. Solidification was carried out by a copper mould casting technique, which yielded a partially crystalline microstructure comprising a 'big cube phase' in a dendritic morphology and a bct Zr_2Ni phase. Detailed high-resolution microscopy was carried out to determine possible mechanisms for the formation of the crystalline phases. Based on microstructural examinations, it was established that the dendrites grew by the attachment of atomistic ledges. The bct Zr_2Ni phase, formed during solidification and crystallisation, showed various types of faults depending on the crystallite size, and its crystallography was examined in detail. It has been shown that the presence of these faults could be explained by anti-site occupancy in the bct lattice of the Zr_2Ni phase.

Keywords: bulk metallic glass; big cube phase; dendrites; Zr_2Ni; transmission electron microscopy (TEM)

1. Introduction

Since the advent of bulk glass in multicomponent Zr-based alloys, a large number of studies have been focused on the formation of various phases in the as-solidified microstructure [1–14]. These as-solidified microstructures in bulk glass-forming alloys can be broadly classified into three categories:

(1) Those showing complete formation of a glassy phase with or without any quenched-in-nuclei of the crystalline phase.
(2) Those which show a composite of nanocrystals and glassy matrix due to limited nucleation followed by very limited growth of crystals.
(3) Those showing few crystals within the amorphous matrix due to limited nucleation but extensive growth of crystals.

Microstructures of type (2) and (3) arise when cooling rates achieved during solidification are lower than the critical cooling rate required for the formation of glass in a system. In bulk glass-forming systems, lowering of cooling rates below the

*Corresponding author. Email: rtewari@barc.gov.in

ISSN 1478–6435 print/ISSN 1478–6443 online

http://dx.doi.org/10.1080/14786435.2012.669061
http://www.tandfonline.com

critical rate will not necessarily lead to the formation of large numbers of crystals as these systems are known for their low steady-state, homogeneous nucleation frequency. The dominating crystallisation event, competing in these systems, is heterogeneous nucleation [15–18]. As a result, upon cooling, crystals, which nucleate on heterogeneous nucleation sites, can grow to different dimensions depending on the prevailing cooling rates and growth rate of the phase. Several characteristic features of the early stages of the solidification process, which are otherwise difficult to observe under normal solidification, are preserved in these partially crystalline solids and can be revealed upon examining the morphology of the crystals embedded in the amorphous matrix.

In Zr-based bulk glass-forming systems, the role of oxygen is critical, as it promotes the formation of oxygen-stabilised phases even when rates of cooling are higher than the critical cooling rate. These phases act as catalytic sites for heterogeneous nucleation of other crystalline phases [19]. This reduces the glass-forming ability of the system substantially. In addition, oxygen also influences the crystallisation behaviour of the glassy phase during ageing of the as-solidified microstructure. In binary TM–Zr metallic glasses (TM = Fe, Ni, Co), oxygen has been found to initiate the crystallisation process via the formation of oxygen-stabilised metastable cubic phases instead of equilibrium compounds [20–23]. The presence of oxygen leading to the formation of the 'big cube phase' or nanocrystallisation of metallic glasses is reported in literature [24–26]. The formation of the 'big cube phase' has also been reported in melt-spun $NiZr_2$ ribbons [22], as well as in bulk glass forming Zr–Al–Cu–Ni alloys [26–28]. Small amounts of oxygen even promote the formation of metastable quasicrystalline phases which act as heterogeneous nuclei for the formation of equilibrium compounds during the crystallisation of metallic glasses [29]. Although the role of oxygen in degrading the glass formability of Zr-based systems is well known, to date, detailed crystallographic studies establishing a mechanism for the role of oxygen in the formation of oxygen-induced crystals have not been carried out.

In this study, the $Zr_{53}Cu_{21}Al_{10}Ni_8Ti_8$ alloy was processed through a copper mould casting technique. The as-solidified structure showed a 'big cube phase', present in a dendritic morphology, and a Zr_2Ni phase with a high density of defects. A detailed microstructural examination was carried out to reveal the atomistic mechanism of solidification of the 'big cube phase' and to characterise and establish the reason and possible mechanism for the formation of defects in the Zr_2Ni phase. The latter also forming during crystallization annealing of the as-solidified alloy was compared with that present in the as-solidified microstructure.

2. Experimental

The $Zr_{53}Cu_{21}Al_{10}Ni_8Ti_8$ alloy was prepared by melting pure elements in stoichiometric amounts in a vacuum arc furnace. To ensure low oxygen content in the alloy, iodide zirconium crystal bars were used. Table 1 shows the composition of the alloy analysed by electron probe microanalyser (EPMA). A copper mould casting technique was selected to synthesise metallic glass in bulk form, wherein pieces of arc-melted buttons were remelted by induction heating and subsequently cast within

Table 1. Composition of the arc-melted button analysed by EPMA.

Zr (at%)	Cu (at%)	Al (at%)	Ni (at%)	Ti (at%)
53.38 ± 1.5	21.1 ± 1.1	9.88 ± 0.6	7.92 ± 0.6	7.72 ± 0.4

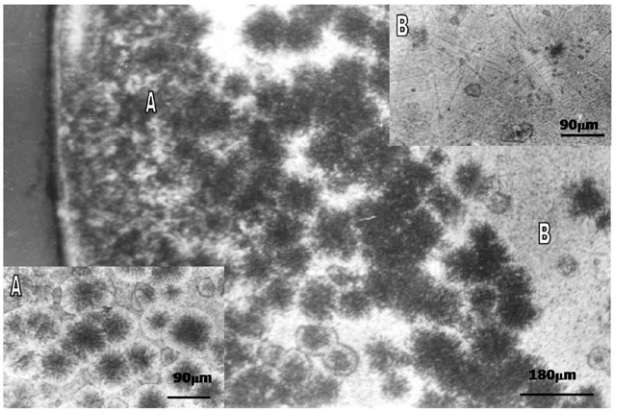

Figure 1. Optical micrograph showing the microstructure of the BMG sample. Note the presence of two regions marked A and B. Inset on top right shows a magnified view of region B, where dendrite arms are seen. Inset on bottom left shows a magnified view of region A, with the presence of a flower-like morphology.

a cylindrical cavity of 6 mm in diameter and 50 mm in length in a Cu mould under a 10^{-3} mbar vacuum. In this technique, oxygen pick-up (2800 ppm of O was measured in the sample) was relatively higher due to the lower level of vacuum in the chamber and also due to pick-up from the silica crucible holding the liquid melt. Bulk glass produced via this route is henceforth referred to as BMG.

The as-solidified structure was characterised using X-ray diffraction (XRD), electron probe microanalysis (EMPA), conventional (CTEM) and high-resolution transmission electron microscopy (HREM). Crystallisation studies were carried out in a differential scanning calorimeter (DSC). TEM specimens of the bulk glass were prepared by a twinjet electropolishing method. The specimens were examined in JEOL 2000 FX and JEOL 3010 transmission electron microscopes. For high-resolution work, samples were cleaned by ion milling in a Gentle Mill^{TM} operating at 0.25 kV. The chemical composition of the various phases was determined by energy dispersive spectrometer (EDS) attached with JEOL 2000 FX.

3. Results

3.1. *Microstructure of as-solidified BMG*

Figure 1 shows an optical micrograph of the microstructure of a cross-section of the BMG sample. The entire cross-section can be broadly divided into two regions

marked A and B on the micrograph. Region B, which appeared nearly featureless at low magnification, showed the presence of a dendritic phase at relatively higher magnification (inset on top right). The peripheral region (marked A) showed the distribution of a phase with a flower-like morphology. The size and density of this phase increased upon moving towards the edge of the sample.

TEM examination of the same specimen shows that the as-solidified microstructure of BMG was comprised of three distinct phases (Figure 2a); the featureless matrix (marked A), the dendritic crystalline phase (marked B) and a crystalline phase having faults of complex morphology (marked C). Selected area electron diffraction

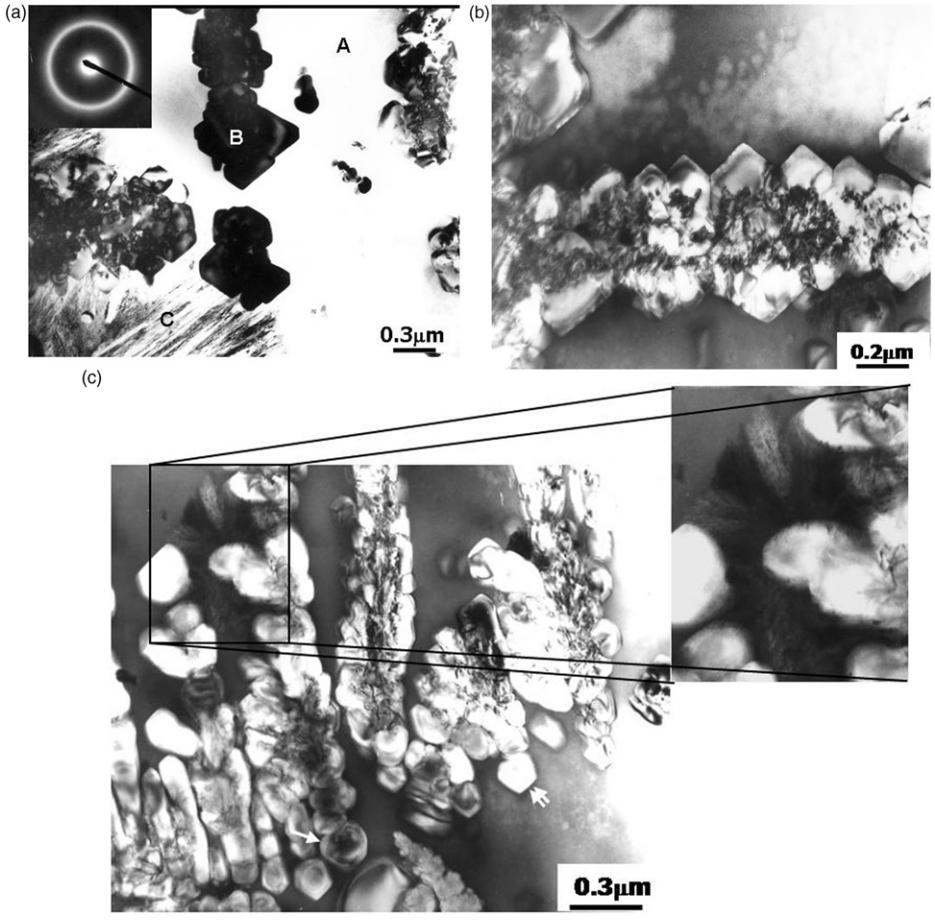

Figure 2. Bright-field TEM micrograph showing (a) the as-solidified microstructure of BMG where regions marked A, B and C represent amorphous, dendrite and faulted phases, respectively. SAED pattern shown in the inset is a halo diffraction pattern obtained from region A, (b) cross-section of the dendritic phase showing the core and faceting of the interface with the amorphous matrix, (c) dendrites exhibiting both faceted and rounded interfaces. Single and double arrows indicate the rounded and faceted interfaces of the dendrites, respectively. Inset shows the faulted crystalline phase present between the dendrites.

(SAED) from the featureless matrix gave a halo pattern (inset in Figure 2a), confirming its amorphous nature. Figure 2b shows the distribution of the dendritic phase with core and primary arms of the dendrite in the amorphous matrix. The presence of a sharp faceted interface could be noticed from this figure. Figure 2c shows another micrograph where dendrites having both faceted and rounded interfaces are noticeable. The faulted crystalline phase, which showed up as flowers at low magnification, could be seen to be present between the dendrites in this micrograph. To understand the distribution of these phases, detailed crystallographic and high resolution microscopy examinations were carried out.

3.1.1. *Dendritic phase and its interface structure*

SAED patterns (one as inset on the top right of Figure 3a), taken from the dendritic phase, could be indexed in terms of a O_h^7 $NiTi_2$ prototype- Zr_2Ni 'big cube phase' (also known as $E9_3$) with lattice parameter ~1.227 nm (space group: $Fd\bar{3}m$). The chemical composition of the dendritic phase determined by EDS showed nominal variation in the bulk concentration of the major elements in the dendritic and interdendritic regions. However, the dendritic phase was found to be enriched with ~7 wt% oxygen compared to negligible oxygen in the interdendritic region.

Detailed HREM analysis of a dendrite arm with a nearly flat interface on one face and a curved interface on the other showed that the flat edges were {111} planes of the 'big cube phase' (Figure 3b). A closer examination of both the faces revealed the presence of several ledges. The density of such ledges was found to be much higher on the curved interface compared to the flat one. Crystallographic analyses between the flat facets in a large number of such interfaces showed that nearly all

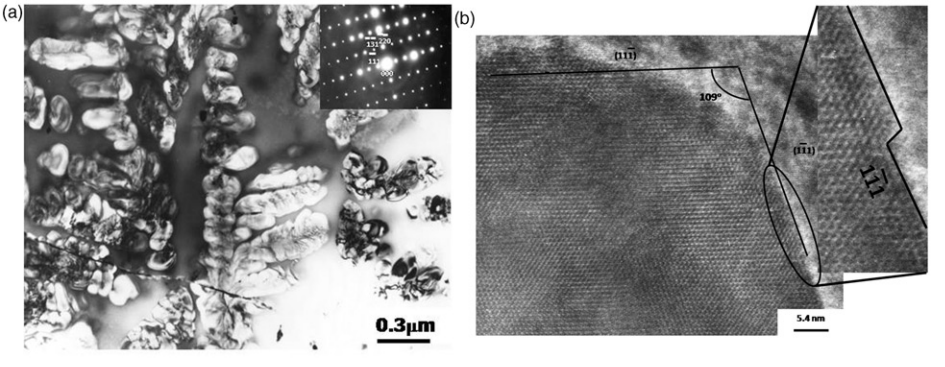

Figure 3. (a) Bright-field TEM micrograph showing the distribution of the dendrites in the amorphous matrix of BMG. SAED pattern (top inset) is from the dendritic phase (zone axis = [$\bar{1}$12]). (b) HREM micrograph showing a dendrite arm having a flat interface on one side and rounded on the other. Ledges can be seen at both the interfaces with a higher density on the rounded one (shown in a magnified view of the marked region). Accumulation of ledges of different widths resulted in the formation of steps at the interface (shown in a magnified view). The lattice planes making up the interfaces correspond to sets of {111} planes as indicated in the figure.

facets are made up of planes belonging to a family of either {111} or {110} or {113} planes.

3.1.2. *Internal structure and interface structure of the faulted phase*

SAED patterns (typical patterns shown as insets in Figure 4a), obtained from the faulted phase, could be indexed in terms of the D_{4h}^{18} body centred tetragonal Zr_2Ni (space group: $I4/mcm$) phase with lattice parameters $a = 0.6483$ nm and $c = 0.5267$ nm. Detailed analyses revealed that each SAED pattern is, in fact, a composite pattern arising due to the superimposition of several variants of the phase. Microdiffractions confirmed such findings as, by combining several microdiffractions with one reciprocal vector ($\langle 110 \rangle^*$) common amongst them, the composite SAED patterns could be reconstructed.

All the SAED patterns obtained from the Zr_2Ni phase were invariably associated with streaking, originating mainly due to the prolate morphology with a high aspect ratio of the coherently scattering domains, exhibited by the faulted phase (Figure 4a). The arrangement of these faults varied in orientation as one moved to different regions. For ease of description, each region having a single orientation of faults will be called a domain in the rest of the text. The domains were found to impinge on each other at different orientations (varying from a few degrees to as high as 90°) within a colony, thus resulting in intersection of streaks in the diffraction patterns at varying angles from a few degrees to 90°. A typical example of impingement of these domains is shown in the bright field-dark field combination of TEM images in Figure 4b where two neighbouring domains (marked 1 and 2) were found to impinge at around 65°. Based on the detailed HREM examination, regions within domains could be divided into three categories:

(1) Regions carrying a high density of faults: In some domains, a uni-directional arrangement of planar faults was noticed (Figure 5a). Most of these faults were atomistically flat. The density of the faults was so high that a typical separation between two faults was in the range 0.5–1 nm. However, the

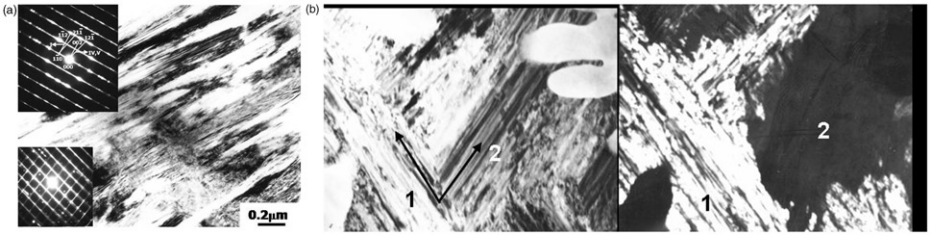

Figure 4. (a) Bright-field TEM micrograph showing the morphology of the faulted phase in BMG. The SAED patterns shown as insets could be indexed in terms of the bct Zr_2Ni phase. The top inset shows a superimposition of three hexagonally oriented twin variants I, IV and V in [110], $[\bar{1}\bar{1}3]$ and $[\bar{1}13]$ orientations, respectively, rotated $\pm 120°$ around $[1\bar{1}0]$. The bottom inset shows superimposition of two sets of [110] and $[1\bar{1}0]$ rotation twins at right angles to each other. (b) Bright-field/dark-field combination of TEM micrographs showing the impingement of two faulted domains (marked 1 and 2) at ~65°. Arrows indicate the orientation of faults in the domains.

separation between the faults was not periodic (as marked by the single arrow in Figure 5a). Crystallographic analyses showed that these fault planes are parallel to the {110} planes.

(2) Regions carrying a low density of faults: In some domains, the fault density was interrupted by relatively flat regions (Figure 5b). Two such regions are marked A and B in this figure. Microdiffractions obtained from these two regions and their interface (shown as insets in Figure 5b) revealed that these regions, which are located side-by-side and separated by a thin interface (~1 nm), have different crystallographic orientations. Detailed analysis confirmed them to be micro-twins having the following orientation relationship (OR): $(\bar{1}10)_A//(\bar{1}10)_B$ and $[11\bar{1}]_A//[001]_B$. In Figure 5b, narrow bands of such micro-twins could be seen at many places. Feng et al. [30] have proposed a $\pm 120^\circ$ rotation twinning around $\langle 110 \rangle$ diad occurring due to anti-site occupancy of Zr and Ni atoms on {110} plane of Zr_2Ni. For a [110] Zr_2Ni crystal orientation, the ORs amongst the three hexagonally oriented twin variants and the ORs existing between these three variants with the variants generated after a $\pm 120^\circ$ rotation around $[1\bar{1}0]$ have been worked out. Similarly, ORs have been worked out for the orthogonally oriented twins for a [001] crystal orientation. These ORs are presented in Table 2. In the present study, microdiffraction and HREM analysis have confirmed the formation of a few of these variants. For example, the top inset in Figure 4a is a SAED pattern comprising hexagonally oriented twins, where superposition of three twin variants I, IV and V has taken place, maintaining the following ORs:

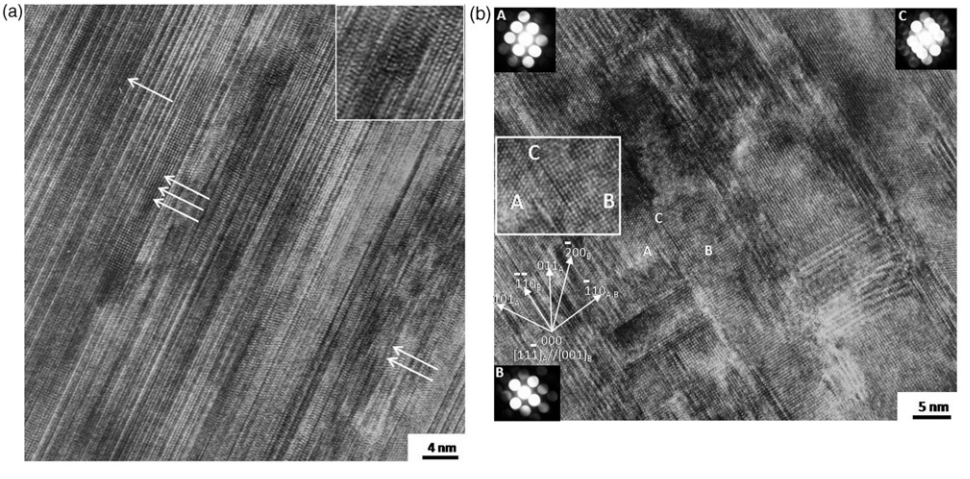

Figure 5. HREM micrographs of the faulted bct Zr_2Ni phase showing (a) arrangement of planar faults within a domain. Single arrow marks an aperiodic distribution of faults in the structure. Double arrows indicates a region carrying a high density of dislocations and the region marked by triple arrows shows the development of a defect-free region by annealing out of faults. The inset shows a magnified view of the dislocated region. (b) Narrow micro-twin bands within a domain where regions A and B represent intergrown twins in $[11\bar{1}]$ and [001] orientations, respectively, with {110} composition plane. The microdiffraction patterns corresponding to regions A, B and C are given as insets. A magnified view of the microtwin variants is also added as an inset.

Table 2. Orientation relationships among twin variants.

[110] Crystal orientation (hexagonally oriented twins)	[001] Crystal orientation (orthogonally oriented twins)
$(1\bar{1}\bar{2})_I//(1\bar{1}\bar{2})_{II}$, $[110]_I//[110]_{II}$ $(1\bar{1}\bar{2})_I//(1\bar{1}\bar{2})_{III}$, $[110]_I//[1\bar{1}0]_{III}$ $(1\bar{1}0)_I//(1\bar{1}\bar{0})_{IV}$, $[110]_I//[\bar{1}\bar{1}\bar{3}]_{IV}$ $(1\bar{1}0)_I//(1\bar{1}0)_V$, $[110]_I//[1\bar{1}\bar{3}]_V$	$(1\bar{1}\bar{0})_I//(1\bar{1}\bar{0})_{IV}$, $[001]_I//[11\bar{1}]_{IV}$ $(1\bar{1}0)_I//(1\bar{1}0)_V$, $[001]_I//[\bar{1}\bar{1}\bar{1}]_V$

$(1\bar{1}0)_I//(1\bar{1}\bar{0})_{IV,V}$ and $[110]_I//[\bar{1}\bar{1}\bar{3}]_{IV}$, $[\bar{1}\bar{1}3]_V$. In fact, the micro-twin bands (A, B) shown in Figure 5b, correspond to orthogonally oriented twins, where superposition of two twin variants, either I and IV (OR: $(1\bar{1}0)_I//(1\bar{1}\bar{0})_{IV}$, $[001]_I//[11\bar{1}]_{IV}$) or I and V (OR: $(1\bar{1}0)_I//(1\bar{1}0)_V$, $[001]_I//[\bar{1}\bar{1}\bar{1}]_V$), has taken place. The SAED pattern in the bottom inset of Figure 4a shows superposition of two sets of orthogonally oriented [110] and1 $[1\bar{1}0]$ rotation twins. In addition to the hexagonal and orthogonal arrangements of variants, as reported by Feng et al. [30], random arrangement of variants was also observed in the present study, which is in agreement with the findings of Liu et al. [31] and Brauer et al. [32].

(3) Regions carrying a high density of dislocations: Such a region is shown by the double arrow in Figure 5(a). Although the presence of a heavy density of faults made it difficult to identify the dislocations, they could be discerned by the discontinuity of atomic planes and also by the presence of strain associated with them, which is manifest by a variation in contrast at the vicinity of the dislocations. Dislocation-like defects were also visible at the boundary of the two aforementioned types of regions.

As during solidification, due to rapid growth of the Zr_2Ni phase, it was not possible to examine the whole crystal in one view under the HREM; therefore, suitable heat treatments through DSC were provided to form nanocrystals of this phase, allowing us to understand its growth mechanism.

Crystallisation of BMG led to the transformation of the leftover amorphous matrix into nanocrystals of the bct Zr_2Ni phase, whereas the dendritic 'big cube phase' and the faulted Zr_2Ni phase, present in the as-solidified microstructure, remained nearly unaffected. Figure 6 shows a high-resolution image of a crystallised nanograin.

In most cases, regions having high dislocation density were found to be located at the periphery, whereas regions of low fault density were formed in the central part of the domains. This situation was more apparent in a crystallised microstructure, where the sizes of such domains were in nanometres. This issue is discussed in the latter part of the paper.

4. Discussion

4.1. *Formation of the 'big cube phase'*

The formation of the $E9_3$ 'big cube phase' in the as-solidified microstructure of BMG is essentially due to oxygen contamination and low cooling rate

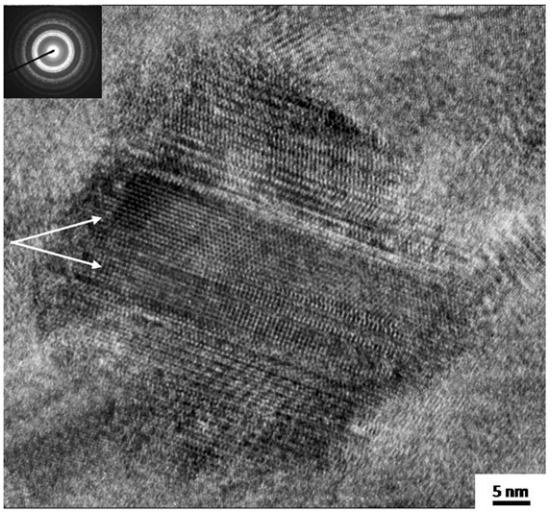

Figure 6. HREM micrograph showing nanocrystal of the bct Zr_2Ni phase in the crystallized microstructure of BMG. Fault-like micro-twin bands (marked by arrows) could be seen within the nanocrystal. The inset is a ring pattern obtained from the nanocrystalline microstructure.

[1–4,22,26–28,33–38]. Altounian et al. [22] have shown that even 1–4 at% O is sufficient to induce the formation of the Zr_4Ni_2O 'big cube phase' in a Zr–Ni-based system. Due to its strong affinity for oxygen, Zr has a tendency to pick oxygen at various stages of fabrication and thus a certain amount of oxygen pick-up is always expected during the synthesis of Zr-based glasses. To understand the mechanism of 'big cube phase' stabilisation by oxygen, it is pertinent to examine the crystal structure of this phase.

The big cube-related phases have $Fd\bar{3}m$ as space group with a unit cell containing 96 atoms (64 Zr and 32 Ni) [33,34]. Figure 7a shows a prospective view of the atomic arrangement in the unit cell of 'big cube phase' from which three points could clearly be noted: (i) Zr atoms form an octahedron, (ii) each Zr octahedron is centred by an oxygen atom (marked in Figure 7a) and (iii) Ni atoms form a tetrahedron (marked in Figure 7a). The size of the Zr octahedron is close to $3.9 \times 10^{-3}\,nm^3$, which is much larger than the volume of one oxygen atom ($\sim 1.6 \times 10^{-3}\,nm^3$). A unit cell of the 'big cube phase', thus, can accommodate up to 16 oxygen atoms without introducing any significant strain in the crystal. However, the formation of 'big cube phase' has been seen in alloys with oxygen concentration as low as 1 at%, suggesting the existence of a wide phase-field for this phase. Typical bond length between Zr and O in such octahedron is nearly 0.21 nm, which matches closely with the bond length of Zr–O in the ZrO_2 structure ($\sim$0.22 nm). Mackay et al. [33] have shown that the presence of oxygen at the octahedral sites lowers the energy of formation of the 'big cube phase' over the Zr_2Ni phase by nearly 137 eV per oxygen atom. Thus, even a small concentration of oxygen is sufficient for the formation of the 'big cube phase'. Figure 7b shows the atomic arrangement of the 'big cube phase' on an {111} plane. As evident from the figure, oxygen atoms lie along one of ⟨110⟩ on an {111} plane, with the least distance between two oxygen atoms on this plane approaching $a/\sqrt{2}$

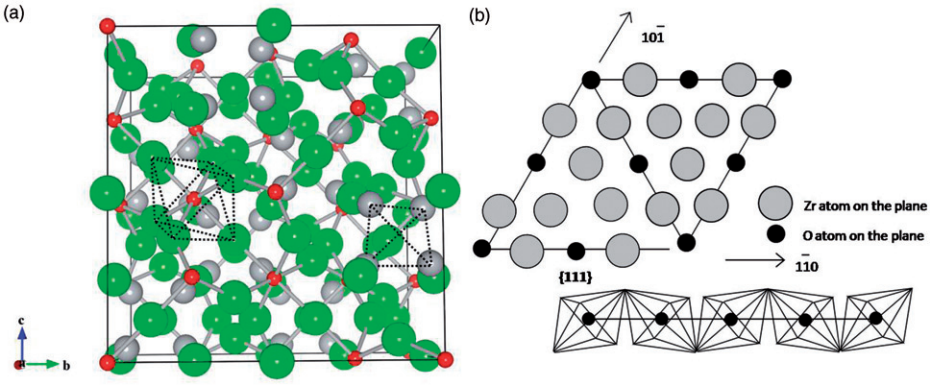

Figure 7. Schematic diagram showing (a) atomic arrangement within a unit cell of the $E9_3$ 'big cube phase'. Zr atoms forming octahedron and Ni atoms forming tetrahedron are marked in the figure. O atoms are seen to occupy the interstitial site within a Zr octahedron. (b) Atomic arrangement on {111} plane of the 'big cube phase'.

(0.867 nm). The arrangement of octahedrons of Zr along the ⟨110⟩ direction is shown in this figure also. Such an arrangement clearly demonstrates that the growth of the 'big cube phase' can be accomplished by quick alignment of octahedrons of Zr, which are stabilised by oxygen, along ⟨110⟩ directions. If a ledge of one step is to be created, the typical height of ledge turns out to be 1.5 nm, which matches closely with the height of ledge observed on flat surfaces in this study. The growth of crystals by a ledge mechanism during solidification is not unusual [39]. Generally, it is observed in cases where a material has a high entropy of fusion [40]. Aziz [41] has proposed an aperiodic stepwise growth model where, if solute partitioning shows strong direction dependence, growth of the solid front depends upon the formation of ledges and on ledge velocity. In the present study, the observation of flat interfaces of the dendrite phase belonging to a family of either {111} or {110} or {113} planes indeed indicates the existence of such low energy interfaces, and the presence of ledges in them points towards a possibility of ledge-based growth of interfaces. This is the first observation of this phenomenon in a metallic glass-forming alloy system.

As the transport of solute is essential for the formation of ledges, and the major alloying elements did not undergo any partitioning during the formation of dendrites, the motion of the interface depended on the diffusion of oxygen towards the interface. A sharp increase in the viscosity of the melt with rapidly decreasing temperature during solidification makes the diffusion of oxygen sluggish. Due to inadequate availability of oxygen atoms, the interfaces either completely stopped or grew marginally with a small concentration of oxygen available in the nearby region, thus causing local instabilities in the solidification front.

4.2. *Formation of the bct Zr_2Ni phase*

The presence of the bct Zr_2Ni phase was noticed in both the as-solidified and crystallised microstructures. The interesting feature associated with this phase is the

presence of fine striations in the microstructure and corresponding streaks in the SAED patterns, which have been explained by many researchers as internal strains [42], stacking faults [43] or micro-twining [44]. Feng et al. [30] gave a geometrical explanation for the combination of different twin variants observed, though the origin behind the high density of faults was unexplained.

A unit cell of Zr_2Ni (C16 $CuAl_2$ type structure) has Zr atoms at 8 *h* and Ni atoms at 4 *a* Wyckoff positions. The positions of Zr atoms can be divided into two categories: one on the 0.25 *z*-plane and the other on the 0.75 *z*-plane. In such a lattice, a defect can occur in two ways:

(1) Change in the stacking sequence of Zr atoms at the 0.75 and 0.25 *z*-planes, as shown in Figure 8a.
(2) Zr and Ni atoms occupying anti-sites in the lattice.

The first type of defect can appear during the growth of the phase if the stacking sequence of Zr atoms changes by the introduction of a fault (½[001]) leading to a twin across {110} planes (Figure 8a). Most of the faults were found to be aligned along ⟨110⟩ (Figures 5a,b and 6). The density of such faults would reach to a maximum when every {110} plane undergoes faulting. Under such a situation, the separation between two faults reaches to a value of 0.458 nm ($\sim d_{110}$), which is close to the fault separation observed in Figure 5a. Peripheral regions of most of the domains, representing a region close to the advancing front, showed relatively high density of such defects (Figures 5a and 6).

Subsequent annealing of defects was achieved by the rearrangement of atoms leading to defect-free central regions in most of the domain (Figure 5b). The presence of such a central defect-free region has also been observed in the Zr_2Ni nanocrystals present in the crystallised microstructures (Figure 6). Figure 5a shows such a defect-free region under development. The rearrangement of atoms on {110} planes can be visualised in Figure 8b. As Zr atoms do not lie on the (110) plane in the lattice of the Zr_2Ni phase, based on their positions with respect to the plane, a (+) or (−) sign has been assigned. Due to a fault, the stacking sequence would change as shown in Figure 8b. A displacement of ½⟨110⟩ (~0.45 nm) is sufficient to anneal out such a stacking defect. In this way, the defect-free region can grow along the thickness in the direction perpendicular to the {110} plane. A displacement along ½[001] can also anneal out these faults, thereby increasing the length of such region.

Figure 5b shows a HREM image where narrow bands having ⟨111⟩ orientations were found to surround relatively larger regions having [001] orientation along ⟨110⟩ directions. Such defects originate when Zr and Ni occupy anti-sites. On an {110} plane, Ni atoms align along the [001] direction. If a Ni atom occupies Zr sites, there are two possible ways it can be accommodated (Figure 8c), thus generating two additional variants with the orientation relationship shown in Table 2. Additional variants also appear from the other $(1\bar{1}0)$ plane. When a growing variant meets with the variant lying on the other {110} plane (these planes are at 90°), they become locked with {111} orientations surrounding the major variant along a common ⟨110⟩ direction. Such {111} orientations were only a few atomic layers thick and contributed to streaking along ⟨110⟩* in the SAED patterns.

There were differences in the nature of the faults present within the Zr_2Ni nanocrystals formed during crystallisation and those present in the as-solidified

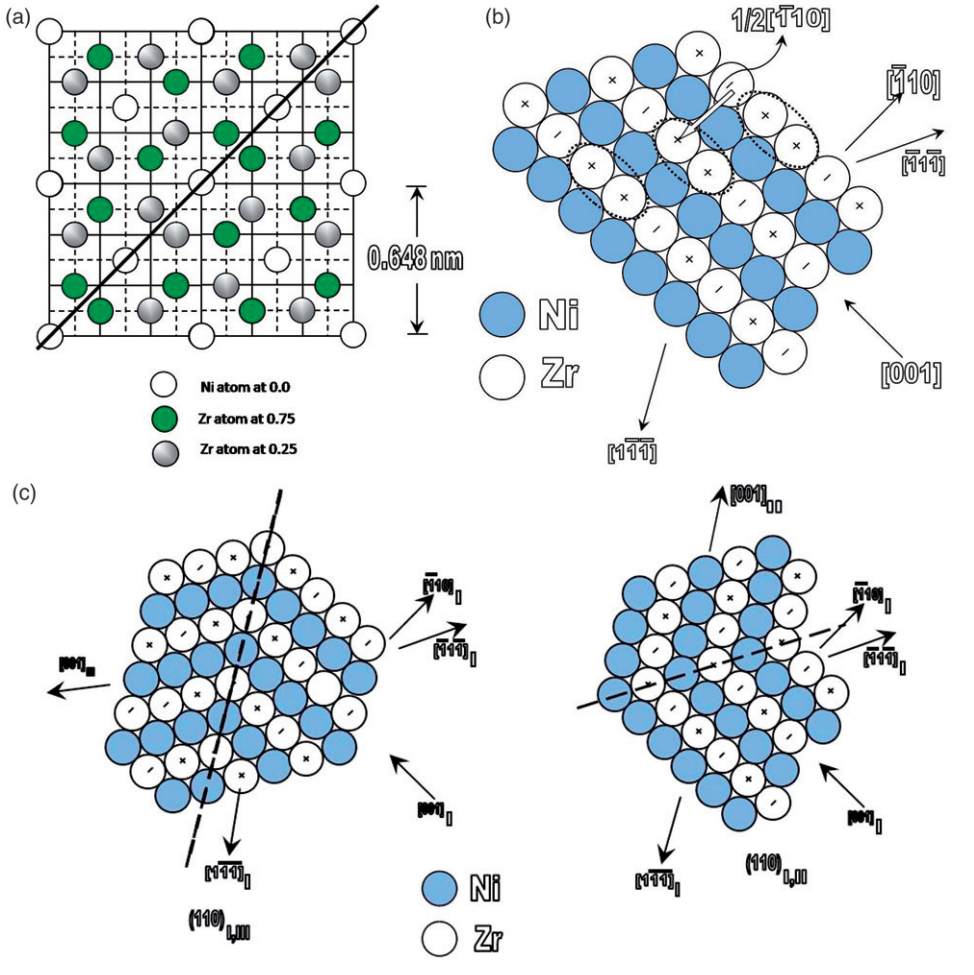

Figure 8. (a) Schematic diagram showing the projection of the bct Zr_2Ni unit cell along [001] direction. The Zr atoms at different z positions (0.25, 0.75) are shaded with different colours. If a fault is introduced in the arrangement of Zr atoms, twinning around (110) plane takes place (marked by thick line). (b) Schematic diagram showing the arrangement of atoms on {110} plane. The + and − signs on the Zr atoms indicate the up and down positions of the atoms with respect to the plane of paper, respectively. The change in the sequence of stacking among Zr atoms has been marked by broken ellipses and the arrow shows the displacement required to restore the stacking sequence. (c) Schematic presentations of twin-variants arising due to the anti-site occupancy of Ni and Zr atoms.

Zr_2Ni phase in BMG. The major differences were that: (i) each nanograin had only one domain, unlike many domains obtained during solidification; in agreement with literature reports (e.g. [45]), and (ii) regions containing dislocations were nearly non-existent in the nanocrystals.

In spite of these aforementioned differences, in either case, thin micro-twin bands were seen (as shown in Figures 5b and 6) indicating a similar mechanism of crystal formation operating in both cases. Taking account of these observations, it can be

conjectured that the early stage of growth of the Zr_2Ni phase is via the formation of a single domain. As the growth process continues, the propensity for faulting increases due to anti-site occupancy by Zr and Ni atoms. Simultaneous growth of these multiple domains increases the propensity for aperiodic faulting (Figure 5). These faults introduce random arrangement of twin variants, in addition to hexagonal and orthogonal arrangements. All these necessitate the formation of different regions, viz. a region of high fault density, a region of low fault density and a region of high dislocation density, within a single domain and their interfaces.

5. Conclusions

In the present study, a detailed transmission electron microscopy investigation of the as-solidified and crystallised microstructures of the $Zr_{53}Cu_{21}Al_{10}Ni_8Ti_8$ bulk metallic glass (BMG), synthesised using a copper mould casting technique, has been systematically carried out. HREM analysis of interfaces of the dendritic 'big cube phase' has shown that the phase grows via the attachment of atomistic ledges during solidification. The ledge density at the interface, which was governed by oxygen content and local conditions of cooling, could also explain the presence of the sharp faceted and curved interfaces of this phase with the amorphous phase.

The faulted Zr_2Ni phase consisted of different domains corresponding to different orientations. A variety of interfaces were noticed between these individual domains and also within a single domain itself. At least three different types of faulted regions were identified to coexist in a single domain. The arrangements of faults and defects were similar in nature in the Zr_2Ni phase formed during solidification or crystallisation. These similarities are essentially due to a similar underlying mechanism for the formation of this phase in each case, which could be explained on the basis of anti-site occupancy by Zr and Ni atoms in the lattice.

References

[1] A. Inoue, T. Zhang and T. Masumoto, Mater. Trans. JIM 31 (1990) p.177.
[2] A. Inoue, T. Zhang and T. Masumoto, Mater. Trans. JIM 31 (1990) p.929.
[3] Z.P. Lu and C.T. Liu, Acta Mater. 50 (2002) p.3501.
[4] A. Inoue, T. Nakamura, N. Nishiyama and T. Masumoto, Mater. Trans. JIM 33 (1992) p.937.
[5] J. Schroers, Acta Mater. 56 (2008) p.471.
[6] A. Inoue, *Bulk Amorphous Alloys*, Trans Tech Publications, Zurich, 1998–99.
[7] A. Inoue, Acta Mater. 48 (2000) p.279.
[8] A. Inoue, H. Tomioka and T. Masumoto, J. Mater. Sci. 18 (1983) p.153.
[9] G. He, Z.F. Zhang, W. Loser, J. Eckert and L. Schultz, Acta Mater. 51 (2003) p.2383.
[10] W.L. Johnson, Mater. Sci. Forum 225–227 (1996) p.35.
[11] A. Inoue, Mater. Sci. Eng. A 304–306 (2001) p.1.
[12] G.K. Dey and S. Banerjee, Metals Mater. Processes 11 (1999) p.305.
[13] C. Suryanarayana, Int. Mater. Rev. 40 (1995) p.41.
[14] W. Chen, Y. Wang, J. Qiang and C. Dong, Acta Mater. 51 (2003) p.1899.
[15] D. Turnbull, Contemp. Phys. 10 (1969) p.473.
[16] A. Inoue, Mater. Sci. Forum 179–181 (1995) p.691.

[17] A. Inoue, Mater. Trans. JIM 36 (1995) p.866.
[18] A. Inoue, Y. Shinohara, Y. Yokohama and T. Masumoto, Mater. Trans. JIM 36 (1995) p.1276.
[19] X.H. Lin, W.L. Johnson and W.K. Rhim, Mater. Trans. JIM 38 (1997) p.473.
[20] I. Ansara, A.K. Pasturel and H.J. Buschow, Phys. Status Solidi (a) 69 (1982) p.447.
[21] Z. Altounian, C.A. Volkert and J.O. Strom-Olsen, J. Appl. Phys. 57 (1985) p.1777.
[22] Z. Altounian, E. Batalla, J.O. Strom-Olsen and J.L. Walter, J. Appl. Phys. 61 (1987) p.149.
[23] U. Koster and J. Meinhardt, Mater. Sci. Eng. A 178 (1994) p.271.
[24] M.M. Nicolaus, H.R. Sinning and F. Haessner, Mater. Sci. Eng. A 150 (1992) p.101.
[25] U. Koster, J. Meinhardt and H. Alves, Mater. Sci. Forum 179–181 (1995) p.533.
[26] U. Koster, J. Meinhardt, S. Roos and A. Rudiger, Mater. Sci. Forum 225–227 (1996) p.311.
[27] P.S. Frankwicz, S. Ram and H.J. Fecht, Mater. Lett. 28 (1996) p.77.
[28] N. Mattern, J. Eckert, M. Seidel, U. Kuhn, S. Doyle and I. Bacher, Mater. Sci. Eng. A 226–228 (1997) p.469.
[29] J. Eckert, N. Mattern, M. Zinkevitch and M. Seidel, Mater. Trans. JIM 39 (1998) p.623.
[30] Y.C. Feng, K.H. Kuo, Z.K. Hei and Y.K. Wu, Philos. Mag. A 56 (1987) p.757.
[31] X.D. Liu, M. Umemoto, W. Deng, L.Y. Xiong, D.H. Ping and K. Lu, J. Appl. Phys. 81 (1997) p.1103.
[32] S. Brauer, J.O. Strom-Olsen, M. Sutton, Y.S. Yang and A. Zaluska, Phys. Rev. B 45 (1992) p.7704.
[33] R. Mackay, G.J. Miller and H.F. Franzen, J. Alloys Compd. 204 (1994) p.109.
[34] J.M. Newsam, A.J. Jacobson, L.E. McCandish and R.S. Polizzotti, J. Solid State Chem. 75 (1988) p.296.
[35] A. Gebert, J. Eckert and L. Schultz, Acta Mater. 56 (1998) p.5475.
[36] U. Koster, D. Zander and R. Janlewing, Mater. Sci. Forum 386 (2001) p.89.
[37] M.F. Oliveira, W.J. Botta, M.J. Kaufman and C.S. Kiminami, J. Non-Cryst. Solids 304 (2002) p.51.
[38] J. Saida and A. Inoue, J. Non-Cryst. Solids 317 (2003) p.97.
[39] M. Asta, C. Beckermann, A. Karma, W. Kurz, R. Napolitano, M. Plapp, G. Purdy, M. Rappaz and R. Trivedi, Acta Mater. 57 (2009) p.941.
[40] A.L. Greer, Mater. Sci. Eng. A 178 (1994) p.113.
[41] M.J. Aziz, Mater. Sci. Eng. A 178 (1994) p.167.
[42] S.H. Van, H.M. Stals and K.H. Buschow, Phys. Statis Solidi (a) 72 (1982) p.153.
[43] M.G. Scott, G. Gregan and Y.D. Dong, in *Proceedings of the 4th International Conference on Rapidly Quenched Metals*, Japan Institute of Metals, Sendai, 1982, p.671.
[44] Y.D. Dong, G. Gregan and M.G. Scott, J. Non-Cryst. Solids 43 (1981) p.403.
[45] X.D. Liu, X.B. Liu and Z. Altounian, Acta Mater. 53 (2005) p.1439.